Detailed Design of a Magnetically-Geared Actuator for use in Extremely Cold Lunar Environments

Justin J. Scheidler[1], Thomas F. Tallerico[1], Aaron, D. Anderson[1], Steven M. Darmon[2], Peter A. Hoge[2], Kyle R. Whitling[2], Jesse Hawk[2], Erica N. Montbach[1]
[1]NASA Glenn Research Center, 21000 Brookpark Rd, Cleveland, OH 44135
[2]HX5, LLC, 3000 Aerospace Parkway, Brook Park, OH 44142
{justin.j.scheidler, thomas.tallerico, aaron.d.anderson-1, peter.a.hoge, kyle.r.whitling, jesse.hawk, erica.n.montbach}@nasa.gov

***Abstract*—A magnetically-geared actuator is being developed for extremely cold space environments to avoid the wiring and significant efficiency penalty associated with heating grease-lubricated actuators as well as the stringent life and loading constraints imposed by dry film lubricated mechanical gears. This paper describes the detailed design of this actuator, including the driving requirements, thermal analysis, bearing loads, electromagnetic analysis and the impact of tolerance stack up, and structural analysis.**

TABLE OF CONTENTS

1. INTRODUCTION

In most state-of-the-art space mechanisms, actuators with mechanical gears are used to rotate components. Grease lubricants are commonly used in space actuators to achieve adequate gear life; however, they require operating temperatures greater than –60 °C. In cold space environments, the need to heat grease lubricants to this temperature can result in effective efficiencies of less than 20% for actuators [1]. Currently, the only flight-proven alternatives to grease lubrication for space actuators are gears made of self-lubricating polymers instead of metal and dry film lubricants like MoS_2. Polymer gears are only viable for light load applications. Dry film lubricants have limiting load and speed requirements to achieve the high end of their life capability. In the nearly pure sliding contact between mechanical gears, one cannot expect dry film lubricants to last more than 1 million tooth encounters [2].

NASA's Motors for Dusty & Extremely Cold Environments (MDECE) Project is developing two rotational actuators that can achieve long life in extremely cold environments without grease lubrication or supplemental heating [3]. One of these actuators is a magnetically-geared actuator. Magnetic gears eliminate the need for gear lubrication by using magnetic fields to transmit torque between rotor bodies instead of physical contact between mating gear teeth. The bearings of the actuator are lubricated with MoS_2 to fully eliminate supplemental heating requirements. The lack of heating helps the actuator achieve a predicted effective efficiency of 86.5% and a life of greater than 5,000 cycles in extremely cold and dusty environments.

It is anticipated that, relative to mechanical gears, magnetic gears are less susceptible to dust contamination, even considering the magnetic constituents that are present in lunar regolith. Although, in dusty environments the bearings in the magnetically-geared actuator are likely to limit the life of the actuator more than the magnetic gears. Experimental evaluation of the actuator's life in dusty environments is a major goal of the project.

A limited number of magnetic gears for space applications have been designed to a limited extent [5] or designed, built, and ground tested to various extents in either ambient [6,7] or cryogenic vacuum environments [8]. The MDECE Project is the first to develop a magnetically-geared actuator for space applications and to explicitly design for the dusty and extreme cold environments of the lunar surface, including permanently shadowed regions.

This paper presents a detailed design of the MDECE magnetically-geared actuator. The actuator consists of an outer stator type magnetically-geared motor [20] connected to a cycloidal type magnetic gear [6]. Section 2 describes the requirements driving the design and their specific impacts. The initial electromagnetic design of the actuator is detailed in Section 3; this includes the characteristics of the cycloidal magnetic gear that lead to high bearing loads and the design changes implemented to reduce those loads and achieve the desired bearing life. A high-fidelity thermal finite element analysis of the actuator is summarized in Section 4. Lessons learned from the thermal analysis are presented, including the operating condition causing the worst-case temperature gradient across key interfaces and components. Section 5 presents electromagnetic analysis of the sensitivity to air gap size, the influence of 3D magnetic effects, and design modifications to reduce mass. Section 6 presents a high-

fidelity structural finite element analysis, including a prediction of the life of each bearing. Conclusions are summarized in Section 7.

2. DRIVING REQUIREMENTS

The magnetically-geared actuator is specified to produce a continuous output of 105 Nm at 2 rpm (22 W power) and a peak output of 208 Nm at up to 1.5 rpm (up to 33 W power) for at least 20 seconds. These requirements are based on a flight qualified reference actuator and are suitable for large robotic arm or rover mobility applications.

The thermal specifications for operation and survival are summarized in Table 1. The cold survival goal is a deep space environment. The cold operating goal is the coldest permanently shadowed region on the lunar south pole. The cold operating and survival requirements are a permanently shadowed region with regolith temperature at the upper limit for water ice to be stable. The hot operating requirement is a laboratory ambient environment. The hot survival requirement is a laboratory ambient environment with assumed ground operations and ground transportation. The hot operating goal is the hottest lunar south pole within 10 km of a permanently shadowed region. The hot survival goal is the hottest lunar equator environment. Across these operating environments the internal actuator temperature ranges from 25 K (-248 °C) to 430 K (157 °C); reference Section 4.

The actuator's operating temperature range motivated the selection of Sm2Co17 magnets. Although less strong than the more popular NdFeB magnets over much of this temperature range, SmCo (1) does not exhibit a rapid decrease in remanent flux density with temperature due to spin reorientation (NdFeB does below 135 K (-138 °C) [13]), (2) exhibits a weaker dependence on temperature both above and below room temperature [14], and (3) is more resistant to radiation [15].

Considering the current TRL of this technology, strict requirements are not imposed on the mass and size. Instead, design objectives were defined based on the aforementioned reference actuator. The design objective for mass is a maximum of 4.73 kg and a goal of less than 3.15 kg. Size is constrained using limits on envelope volume (a maximum of 1440 cm^3 and a goal of less than 960 cm^3) and length-to-diameter aspect ratio (between 0.5 and 1.75).

The key performance parameters of the MDECE Project were previously detailed in [1].

3. INITIAL ELECTROMECHANICAL DESIGN

Both the cycloidal output stage and the outer stator magnetically-geared motor (OSMGM) were designed using genetic optimizations based on static 2D finite element analysis. Torque margins were imposed on both designs to account for 3D leakage of magnetic flux and manufacturing defects. A 20 % margin was applied to the cycloidal design, whereas a 10% margin and a 3D leakage correction based on [16] was applied to the OSMGM.

A nominal air gap of 0.25 mm was selected for both the cycloidal gear and the OSMGM based on preliminary analysis.

Cycloidal Magnetic Gear

For the cycloidal gear optimization, a code was developed that evaluated the magnetic and mechanical performance of different cycloidal gear geometries selected by the genetic algorithm. In a cycloidal magnetic gear, the forces generated by the eccentric rotor on the bearings is a major driver of both the mass and efficiency of the gear stage. The eccentricity causes significant radial magnetic force and the cycloidal gear's input torque to transfer through the eccentric bearing. The eccentricity also necessitates that the output torque is transferred from the eccentric rotor to the output shaft through a connection that has an equal and opposite eccentricity. Both dry-film-lubricated pins and needle bearings were evaluated for this connection. Pins take up significantly less volume and have a less complex mechanical design than needle bearings. However, pins have only one point of contact with the eccentric member and correspondingly can only be loaded in the direction of eccentricity. Conversely, needle bearings have several rollers in contact with the eccentric member and can transfer load in all radial directions. Consequently, for a given number of connections, pins are exposed to higher peak loads and typically have higher contact stress. Needle bearings also considerably reduce the amount of sliding at the contacts relative to pins, which reduces loss and should improve the dry film lubricant's life.

Table 1. Thermal specifications for the MDECE magnetically-geared actuator.

Parameter	Condition	Specification			
		Minimum		Maximum	
		Goal	Required	Required	Goal
Lunar surface temperature	Operating	30 K (-243 °C) [9]	108 K (-165 °C) [10,11]	293 K (20 °C)	313 K (40 °C) [12]
	Survival	3 K (-270 °C) [9]	108 K (-165 °C) [10,11]	293 K (20 °C)	393 K (120 °C) [9]
Solar heating environment	Operating	Shadowed	Shadowed	N/A	Lunar south pole (85° S)
	Survival	Shadowed	Shadowed	N/A	Lunar equator

Figure 1 depicts an example cycloidal magnetic gear and the forces acting on its eccentric rotor at a snapshot in time. This example has three pins that each transfer force between the eccentric rotor and output shaft through a sliding contact.

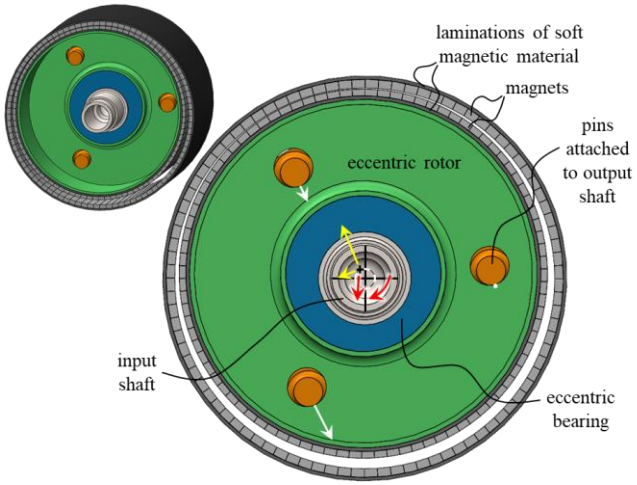

Figure 1. Example cycloidal magnetic gear (housing hidden) with sliding pin contact showing the loads on the eccentric rotor: net radial magnetic force and torque (red arrows), contact force between pins and eccentric rotor (white arrows), and load through eccentric bearing (yellow arrows); eccentric rotor's center (small black cross) orbits the gear's main axis (large black cross) around the dashed white circle of radius equal to the eccentricity.

The force on each eccentric connection depends on the number of pins, whether sliding pins or needle bearings are used, and the output torque. Figure 2 demonstrates this relationship. Needle bearings are shown to reduce the pin force by about half. Adding pins always reduces the peak pin force with diminishing returns.

A portion of the magnetic and pin loads are passed to the bearings in the actuator. Hence, the loading of each bearing is also driven by the selection of sliding pins or needle bearings. This influence is significant for the eccentric bearing, as shown in Figure 3. Note that in all cases, the force on the eccentric bearing is relatively large even when the gear is unloaded, because of the unbalanced radial magnetic force.

The magnitude of the pin and bearing forces makes it challenging to balance the life of dry film lubricants and the size and mass of bearings. The challenge is complicated by the time-varying nature of the forces, which are depicted in Figure 4 for an example case. The force on each pin varies with time regardless of number of pins and contact type. The force on the eccentric bearing varies with time for sliding pins but not for needle bearings.

Within the optimization of the cycloidal stage, the loss and weight of the bearings were accounted for. The design code developed for this magnetically-geared actuator includes an optimization of the bearing selection for each ball and needle

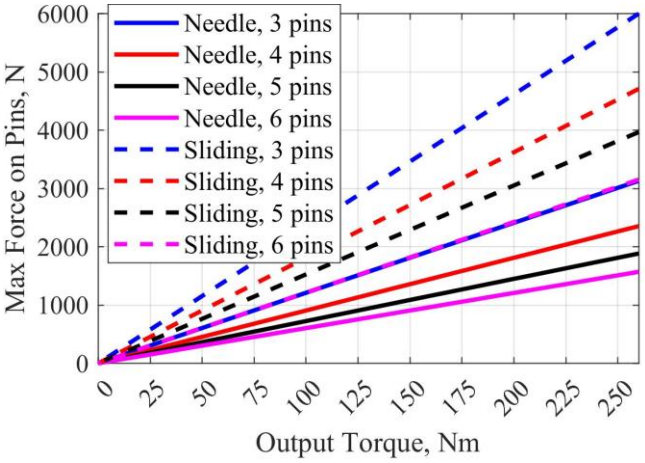

Figure 2. Dependence of the maximum force on the pins in the preliminary geometry of the cycloidal magnetic gear as a function of the load torque for different number of pins and for sliding contact pins and needle bearings.

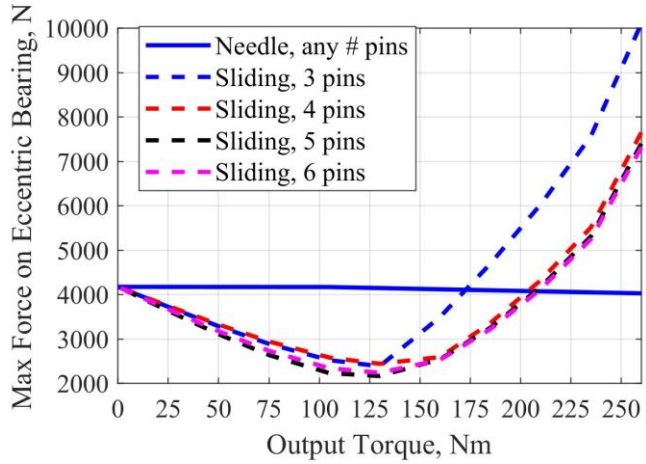

Figure 3. Dependence of the maximum force on the eccentric bearing in the preliminary geometry of the cycloidal magnetic gear as a function of the load torque for different number of pins and for sliding contact pins and needle bearings.

roller bearing in the actuator. This optimization considers, among other things, the aforementioned pin and bearing loads, axial preload on angular contact ball bearings, and a catalog of off-the-shelf bearings. The contact stress, life of dry film lubricant, and frictional power loss due to sliding at each rolling element-raceway contact were calculated for each bearing option in the catalog at each bearing in the actuator. The catalog bearing that provided the best combination of life and loss was selected for each bearing in the actuator.

Figure 5 presents the Pareto front of the cycloidal gear for the case of 3 sliding contact pins and for needle bearings with different number of pins. With pins in sliding contact, the cycloidal gear is found to be less efficient and considerably heavier than when needle bearings are used. A design based on needle bearings with 4 pins was selected due to the

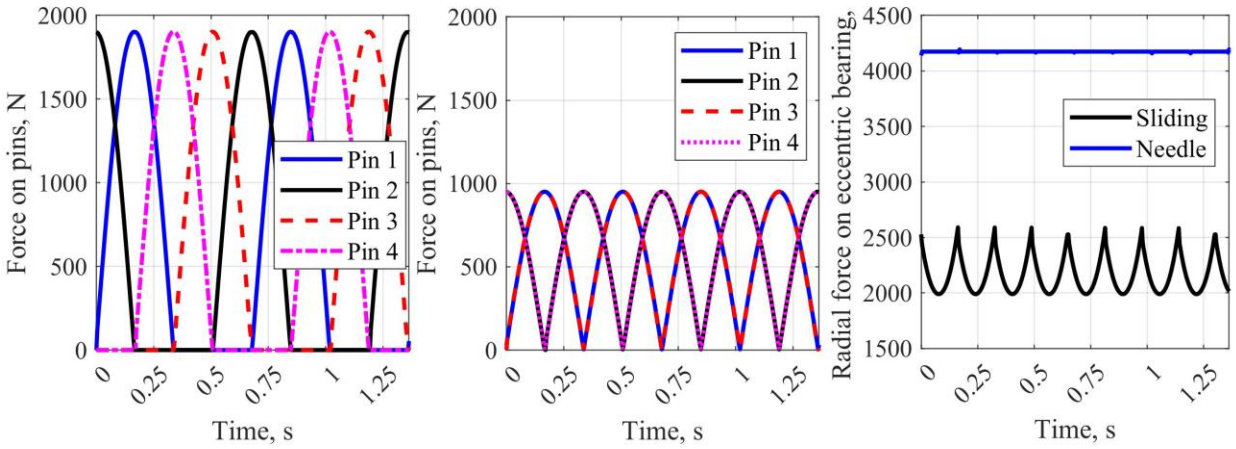

Figure 4. Time dependence of the force on each pin in the preliminary geometry of the cycloidal magnetic gear at the continuous operating condition (105 Nm output torque) for sliding contact pins (left) and needle bearings (center) and on the eccentric bearing (right).

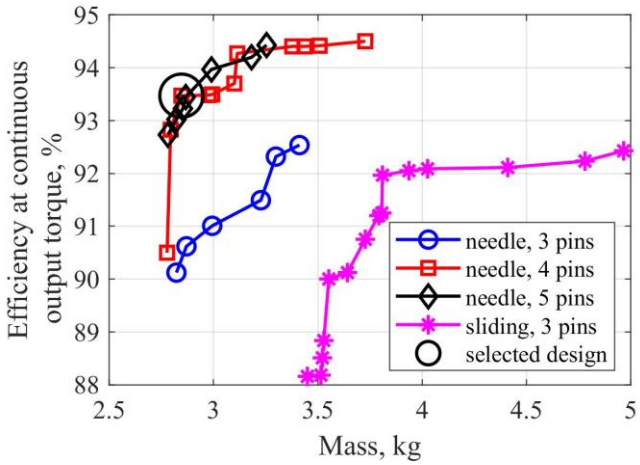

Figure 5. Pareto fronts from genetic optimization of the cycloidal magnetic gear for 3 sliding contact pins and for needle bearings with different number of pins.

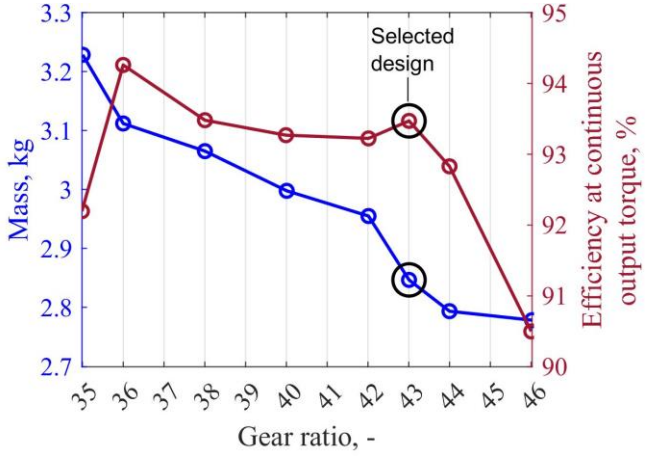

Figure 6. Optimal mass and efficiency (with no torque margin) of the cycloidal magnetic gear with needle bearings and 4 pins as a function of its gear ratio.

increased performance relative to 3 pins and the decreased complexity compared to 5 pins.

Since only the output speed of the actuator (i.e., of the cycloidal gear) is constrained, the gear ratio of the cycloidal gear and of the magnetically-geared motor are independent variables. To ensure the actuator as a whole is optimized, the cycloidal gear was optimized first and the highest performance design at several gear ratios was extracted. Figure 6 depicts this result. The optimal combination of efficiency and mass of the cycloidal gear as a function of its gear ratio was then used to represent the cycloidal gear in the optimization process of the magnetically-geared motor. A design with a gear ratio of 43:1, a mass of 2.85 kg, and a continuous efficiency of 91.9% was selected.

Magnetically-Geared Motor

The OSMGM was optimized using an edited version of the code presented in [20]. The OSMGM was sized to produce 110% of the required input torque for the cycloidal stage. $208/GR_{\mathrm{cyc}}/\eta_{\mathrm{cyc}}$ where GR_{cyc} and η_{cyc} respectively are the cycloidal gear's gear ratio and predicted efficiency at peak operating conditions. The results of the design optimization are shown in Figure 7. From the results, a design with a gear ratio of 13:1, a mass of 0.89 kg, and a continuous efficiency of 91.3% was selected. To reduce torque ripple while not adding additional radial bearing loads, the gear ratio of the design was increased to a non-integer value of 13.5:1. A higher fidelity efficiency analysis was then completed using pseudo time stepping finite element analysis as described in [20] to obtain the loss estimates given in Table 2. Losses were similarly evaluated for the cycloidal stage. They are also summarized in Table 2.

The mass and continuous efficiency of the initial actuator design predicted by the design codes are 3.74 kg and 83.9% (including the torque margins).

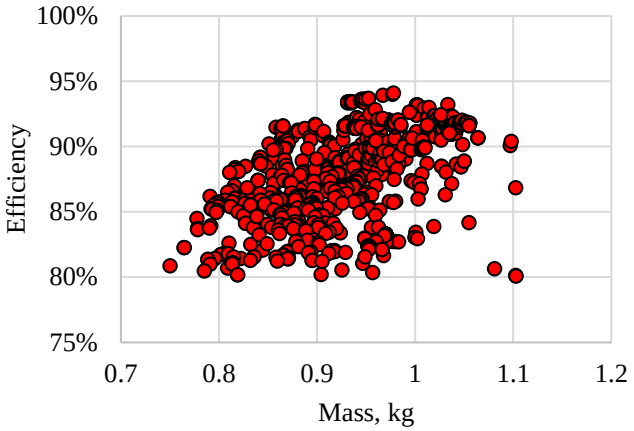

Figure 7. Results from the design optimization of the outer stator magnetically-geared motor.

4. THERMAL ANALYSIS

The actuator was analyzed in all environments specified in Table 1, including lunar permanently shadowed regions, lunar sunlit regions, and laboratory vacuum test environment. For the lunar environments, the lunar surface was modeled with a constant surface temperature and optical properties from [17]. The constant temperature assumption dictates that the actuator and the system it is connected to has a negligible impact on the local regolith temperature. No other hardware (rover, lander, etc.) was modeled. The thermal model is shown in Figure 8. The actuator's bearings were not modeled explicitly but rather as an effective thermal conductance. Each bearing's heat load was applied in an area-weighted manner at its inner and outer diameter. Input and output shafts were assumed to be adiabatic.

Temperature-dependent material properties were included where data is available or where a reasonable estimate could be determined from room temperature data and a known trend with temperature. Temperature-dependent thermal conductivity and specific heat was found for all materials except the bearing materials, permanent magnets, epoxy, and a material used for a couple of structural parts. Cryogenic emissivity data could not be found, but measurements are in progress for a few key materials.

The heat loads applied in the model are tabulated in Table 2. Time-averaged heat loads in every ball bearing were calculated based on the shear strength of the MoS_2 dry film lubricant and the sliding friction moment at each ball-raceway contact. Heat loads due to friction between the rolling elements and the cage were neglected. For the needle bearings in this analysis, the heat load was estimated by applying a factor of safety of three to the losses predicted using equations for *grease-lubricated* needle bearings. This estimate is expected to be a conservative estimate. The heat produced by the dust seals – estimated to be 25 mW per seal – is not included in the following analysis but is expected to have a minimal influence. The authors are currently revising the thermal model to include needle bearing heat loads calculated from sliding friction moment, temperature-dependent bearing heat loads that result from differential thermal expansion, temperature-dependent stator coil and permanent magnet heat loads, and dust seal heat loads.

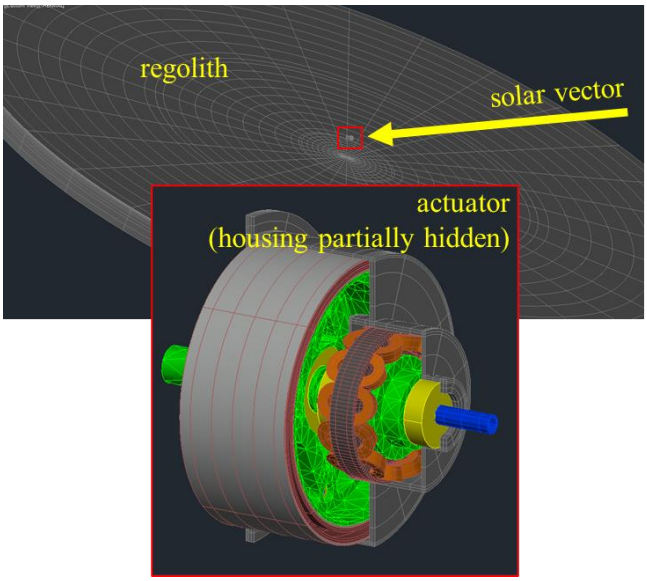

Figure 8. Thermal model of the magnetically-geared actuator on the lunar surface; condition depicted is the hot operating goal, in which the regolith surface is tilted 21° toward the sun because the 40 °C surface temperature only occurs on crater slopes or hills.

Table 2. Heat loads (units of mW) for the preliminary magnetically-geared actuator under continuous and peak operating conditions.

		Continuous	Peak
Cycloidal gear	Bearing 1	34.8	23.8
	Bearing 2	1.1	0.7
	Bearing 3	48.7	33.3
	Needle bearings	1843 (est.)	2738 (est.)
	Inner magnets	< 0.1	< 0.1
	Outer magnets	< 0.1	< 0.1
Magnetically-geared motor	Bearing 1	7.5	7.5
	Bearing 2	0.6	0.6
	Bearing 3	0.6	0.6
	Bearing 4	7.5	7.5
	Stator coils	1301	5587
	Stator iron	750	465
	Modulator	80	50
	Ring magnets	83.6	46.7
	Sun magnets	86.4	50
Total		4245	9011

The surface finish or coating of external housing surfaces is a design choice with thermal implications. Coatings with a lower absorptivity-to-emissivity ratio result in cooler temperatures when the actuator is exposed to solar radiation, but they may not be rated for cryogenic temperatures. Since the actuator is designed to tolerate cryogenic temperatures, a higher emissivity is preferred to improve cooling in shadowed conditions. In the current design, a generic anodized titanium finish is specified to ensure compatibility at cryogenic temperatures while still providing an absorptivity-to-emissivity ratio less than bare titanium.

Due to radiative cooling to space, the actuator reaches a minimum temperature of 25 K (-248 °C) in the cold operating goal environment before operation begins. After operating until steady state is reached, the actuator reaches the temperature distribution shown in Figure 9. The hottest components are the pins that transfer load between each pair of needle bearings, due to the heat produced in the needle bearings and the indirect heat transfer path to the housing. If, as expected, the needle bearing heat load markedly reduces with further refinement, the hottest components would become the stator and modulator in the magnetically-geared motor.

Figure 10 depicts the steady state temperature distribution under a worst-case hot condition (hot operating goal environment under *infinite duration* peak operating conditions). Thus, the results presented are conservative, because the actuator is only required to maintain peak operation for 20 seconds. In this case, the heat load in the magnetically-geared motor's stator dominates the others. Consequently, the magnetically-geared motor is about 20 to 35 °C warmer than the cycloidal magnetic gear despite the stator's relatively direct heat transfer path to the actuator's housing (i.e., the radiator). Ongoing analysis is evaluating the actual operating conditions by first obtaining a steady state response with continuous operation heat loads and then running a ≥ 20 s transient response with peak operation heat loads. The results of this new analysis suggest that the temperature rise during the short transient will be small – about 2 °C – and that the conservative case considered in Figure 10 overpredicts the temperature in the cycloidal gear and geared motor by approximately 15-20 °C and 20-30 °C, respectively.

Temperature gradients inside the actuator cause relative displacement between rotors and stationary components and can cause thermally-induced stresses inside bearings. Thermal transient analysis was completed to quantify transient thermal gradients and ascertain the thermal condition for which the gradient across each air gap and bearing is largest. Table 3 summarizes the worst-case thermal gradient across each point of concern in the actuator and the condition at which it occurs. For most points of concern, a transient condition results in the largest temperature gradient.

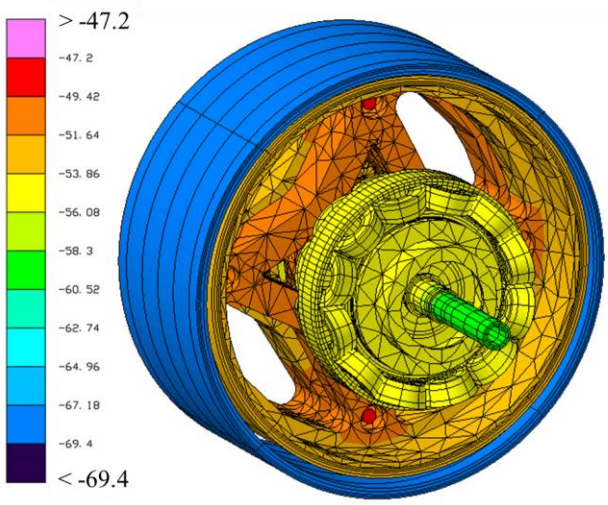

Figure 9. Steady-state temperature distribution (°C) of the preliminary magnetically-geared actuator in the cold operating goal environment under continuous operating conditions.

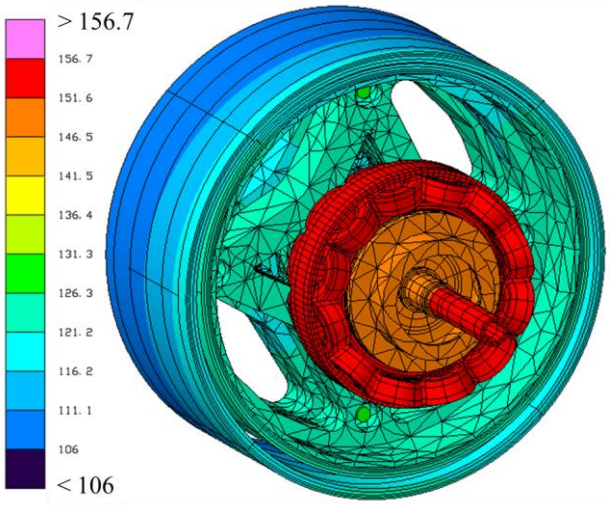

Figure 10. Steady-state temperature distribution (°C) of the preliminary magnetically-geared actuator in the hot operating goal environment under peak operating conditions.

As shown in Table 3, there is a relatively large temperature gradient across the air gap in the cycloidal gear and across the air gap between the stator and modulator in the magnetically-geared motor. Structural analysis of these components will include the differential thermal contraction at these conditions to ensure the gradient does not significantly reduce the already small nominal air gap. The temperature gradient across three of the needle bearings is also significant. Before the actuator's design is finalized, each bearing will be re-optimized accounting for the worst case temperature gradient in order to assure sufficient life and power loss is achieved.

Table 3. Worst case temperature gradients in the preliminary magnetically-geared actuator.

Area of concern	Operating condition	Temperature gradient, K
Air gap 1	Steady state	2.3
Air gap 2	Transient warm-up	19.0
Air gap 3	Transient warm-up	18.6
Bearing 1	Transient warm-up	3.2
Bearing 2	Transient warm-up	2.5
Bearing 3	Transient warm-up	2.7
Bearing 4	Transient cool-down	2.8
Bearing 5	Transient cool-down	1.8
Bearing 6	Transient warm-up	2.1
Bearings 7-10	Transient warm-up	6.9
Bearings 11-14	Transient warm-up	14.4
Bearing 15	Steady state	6.8

Several bearings are predicted to have a small thermal gradient throughout all operating conditions. Although, one key area of refinement for the thermal results presented here is the bearing thermal conductance. Results in this section were obtained using generic thermal conductances of appropriate magnitude for room temperature operation. Data in [18] demonstrates that thermal conductance of dry film lubricated bearings decreases by about an order of magnitude from room temperature to low cryogenic temperatures. Work is ongoing to calculate the thermal conductance of each bearing as a function of temperature based on cryogenic material properties and the actual contact area at each contact between rolling element and raceway. The resulting thermal conductance predictions will be incorporated into future thermal analysis of the actuator.

5. Additional Electromagnetic Analysis

After the completion of the initial design, three additional electromagnetic analyses were completed: an airgap sensitivity study, sizing of the cycloidal's back iron, and 3D leakage analysis.

Early in the design process for the cycloidal magnetic gear it was assumed that the magnet arrays required a back iron to increase specific torque and prevent excess eddy current loss in the surrounding structure. The gear's electromagnetic performance and mass were optimized with a $Fe_{49.5}Co_{48.5}V_2$ lamination stack back iron included on each magnet array. The radial thickness of each stack was constrained to be ≥1 mm to account for manufacturing limitations. The genetic optimization of the cycloidal gear pushed the design to this lower limit of 1 mm. Initial electromagnetic analysis of the design suggested that due to the low electrical frequency of the cycloidal gear and the use of Halbach arrays, very little flux leakage and loss would occur in the surrounding structure without the iron. Thus, an additional electromagnetic analysis of the design was completed to quantify the change in torque that would occur if either or both of the lamination stacks was eliminated (i.e., the structure was resized to directly mate with the magnets) or replaced by extra permanent magnet material. Table 4 presents the percent change in the actuator's output torque per meter of axial length that would occur in each case. A minimal reduction in torque per meter is observed when the lamination stacks are eliminated, whereas a considerable increase in torque occurs when the stacks are replaced by larger magnets. To compensate for the increase or decrease in torque per meter in each case, the axial length of the gear was scaled so that the required output torque was maintained. The resulting percent change in the actuator's total mass is summarized in Table 4. In all cases, eliminating the iron results in a mass reduction. The largest reduction is shown to occur when the irons are eliminated. Further analysis and refinement of loss and mass predictions with and without iron is the target of ongoing work.

Table 4. Percent change in the actuator's output torque (T) due to eliminating the inner and outer iron lamination stacks in the cycloidal magnetic gear or replacing them with extra permanent magnet material; also, the resulting *approximate* percent change in the actuator's total mass (m) after adjusting the cycloidal gear's length to maintain a fixed output torque.

		Inner rotor		
		No iron	**Baseline (iron)**	**Magnet**
Outer stator	**No iron**	T: –0.6% m: –11.3%	T: –0.1% m: –6.2%	-
	Baseline (iron)	T: –0.7% m: –5.1%	0%	T: +18.5% m: –1.2%
	Magnet	-	T: +15.9% m: –1.0%	T: +37.6% m: –2.5%

As mentioned above, in order to meet the mass target for the actuator, the magnetic gears were designed with a small air gap of 0.25 mm. Based on a tolerance stack up analysis of the actuator, the air gap in practice may vary from this nominal value by +/- 0.085 mm in the cycloidal gear and +/- 0.036 mm in the OSMGM. Electromagnetic analysis was completed on each component to quantify the percent change in torque that would result from this level of variation of the actual air gap. Figure 11 summarizes the results. The nominal air gap size and expected tolerance range are shown for each component on the plots. For the cycloidal results, cases A, B, and C in Figure 11a refer to three different ways in which a change in air gap could occur. The cycloidal gear is found to be relatively insensitive to changes in air gap, well within the 20% margin included in the design. The OSMGM is shown to be significantly more sensitive to variations in air gap; however, it has a much smaller expected range on its nominal air gap and should stay under the 10% margin

included in its design. Further refinement of the variation in the air gap, including variations due to thermal transients, is the target of future analysis.

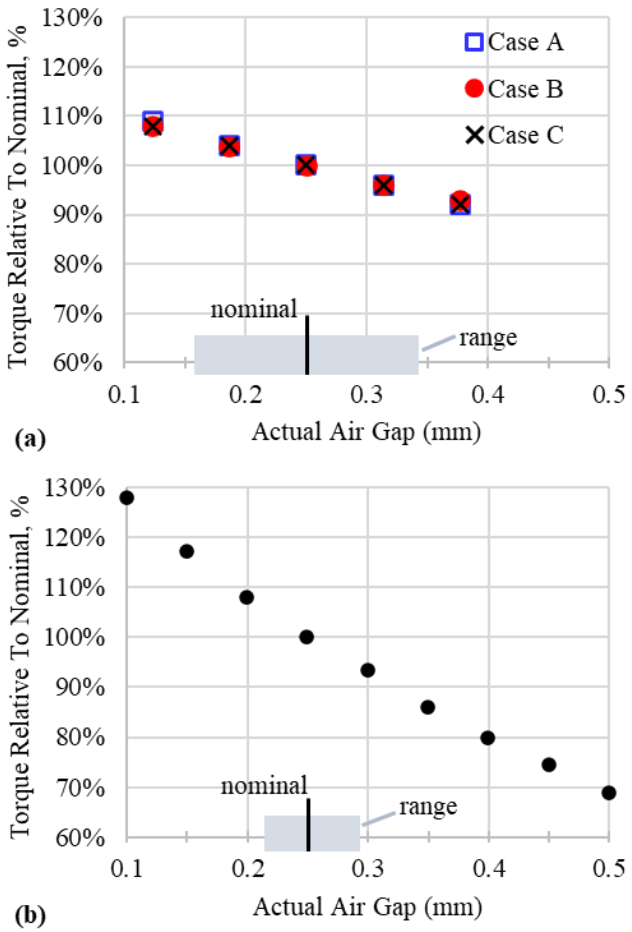

Figure 11. Influence of air gap on the 2D predicted torque of the (a) cycloidal magnetic gear and (b) magnetically-geared motor; gray box depicts the expected range of air gap due to tolerance stack up.

It is well established that 2D finite element models of magnetic gears overpredict the torque capability of the gears since they neglect 3D magnetic flux leakage [19]. Concentric magnetic gears like that contained in the magnetically-geared motor are particularly affected by 3D leakage. The overprediction of the OSMGM's torque using 2D finite element analysis was compensated for in the design process by using the data in [19]. Accounting for a 10% margin on the geared motor's output torque, a 20% margin on the cycloidal gear's output torque, and the inefficiency of the cycloidal gear, the motor must output a peak torque of 5.68 Nm. Based on an estimated overprediction of 34.5%, the geared motor was designed to produce 7.64 Nm peak torque according to a 2D simulation. A 3D electromagnetic simulation was then used to quantify the actual torque for the chosen design of the geared motor. The actual torque was found to be 5.82 Nm, or only 2.5% greater than the target, indicating that the results in [19] provide an accurate correlation in this case.

A 3D analysis of the chosen cycloidal magnetic gear was also conducted, indicating an output torque of 268.5 Nm. The 2D analysis of the same design predicts a 271.0 Nm torque, which corresponds to an overprediction of only 1%. Although, if the number of eccentric rotors is increased from 1 to 2 or 3 as proposed in [6] to reduce bearing loads, the 2D model overpredicts the output torque by 3.2% (270.1 Nm compared to 262.4 Nm) or 5.5% (270.1 Nm compared to 257 Nm).

6. Structural Analysis

A high fidelity structural finite element analysis of the preliminary magnetically-geared actuator design was completed. In all cases, the loading corresponded to the peak operating conditions. The meshed geometry is shown in Figure 12. The thermal conditions considered were room temperature, at the start of cold operation (the coldest condition), and steady state worst-case hot operation. For computational efficiency, the temperature dependent thermal expansion coefficient of each material was not included. Rather, the average temperature of each component was extracted from the thermal analysis for each thermal condition, and then a secant coefficient of thermal expansion was defined for each component such that it yielded the correct thermal strain at the temperature of interest.

The loads considered in the model include: thermal forces due to differential thermal expansion/contraction; the radial magnetic force on each modulator pole piece and magnet in the magnetically-geared motor; the magnetic force on each magnet in the cycloidal magnetic gear; torque on the modulator and ring magnets in the magnetically-geared motor (the net torque on the sun gear is zero); and the centrifugal load on the modulator and sun rotor in the magnetically-geared motor. The centrifugal forces inside the cycloidal gear are neglected due to the inclusion of a counterbalance to offset the eccentric rotor's mass eccentricity and the low speeds (up to 2 rpm output and 86 rpm input). No relative displacement across epoxied interfaces was allowed. The calculated bearing stiffnesses consider the geometry of the bearing and applied loads. Each bearing was modeled as a generalized spring damper structural scalar element.

An important output from the model is the deformation of the components located adjacent to each air gap. In the magnetically-geared motor, the radial deformation of these components was found to not be a concern due to the small magnitude of the non-torsional forces in the geared motor. In the cycloidal magnetic gear, radial deformation of the surface of the inner magnets on the eccentric rotor and the surface of the outer magnets is appreciable. Figure 13 depicts the nominal air gap in the cycloidal gear as a function of circumferential position around the gap, as well as the calculated change in air gap due to structural deformation.

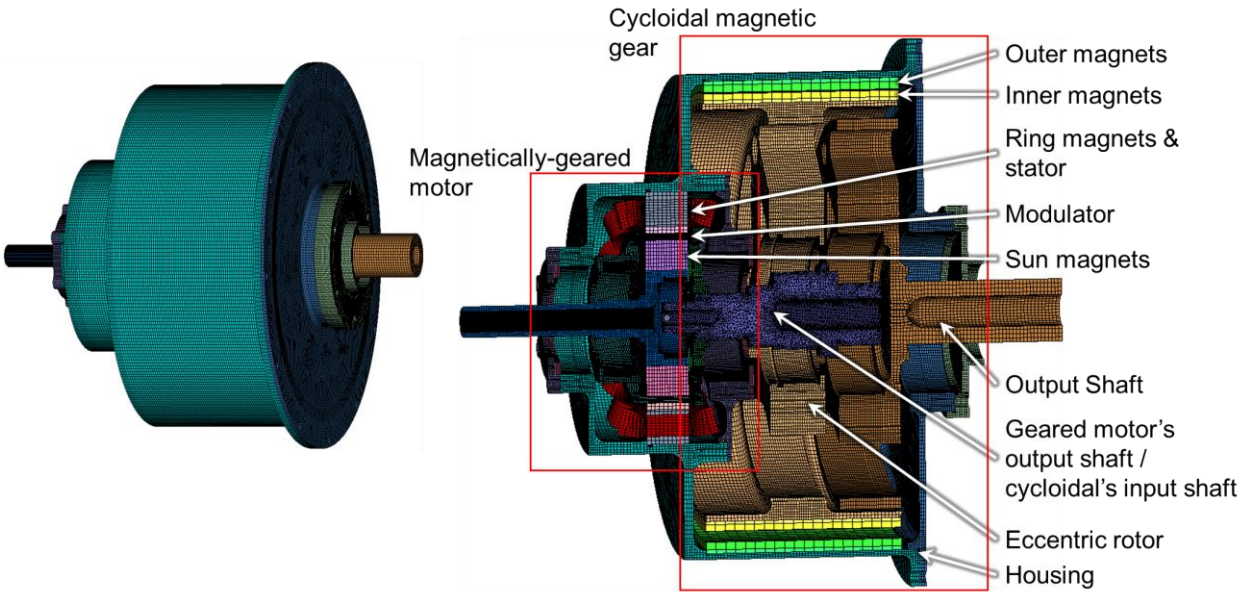

Figure 12. Finite element mesh for structural analysis of the preliminary magnetically-geared actuator (bearing stiffness elements not shown for clarity).

The magnitude of the change in air gap is significant compared to the minimum air gap (0.25 mm). However, the maximum change occurs about 90° away from the location of minimum air gap. Consequently, the minimum air gap in the deformed state is 0.23 mm, 0.25 mm, and 0.26 mm for the cold, room temperature, and hot cases, respectively. The results indicate that the change in air gap is dominated by the non-thermal forces, because the change in air gap is minimally affected by the thermal condition.

Factors of safety for the structural analysis were taken from NASA-STD-5001B [19]. The stress analysis of the preliminary actuator indicates that all margins are positive at room temperature. At the coldest condition, negative margins were observed in the stator iron, stator coils, and ring magnets. However, at this time the stator coils are treated as bulk pieces of solid copper in the model of the whole actuator for computational efficiency. Thus, a higher fidelity structural analysis of only the stator was conducted. This higher fidelity model considers each turn of the stator coils and the epoxy used to join them together and to the stator iron. Results from the higher fidelity model indicate that all margins are positive when the epoxy is properly designed. Including the results of this more detailed stator coil, all structural margins are positive.

Bearing forces were also extracted from the structural analysis and used to refine the life estimate for each bearing. Table 5 summarizes the results, indicating that the threshold value for bearing life is being achieved by all but one bearing. However, only one bearing is predicted to achieve the goal life of the actuator. Although the key performance parameters of the actuator [1] do not consider the bearing life because the project is not attempting

to improve the state-of-the-art in cryogenic bearings, higher bearing life is desired to improve the usefulness of this

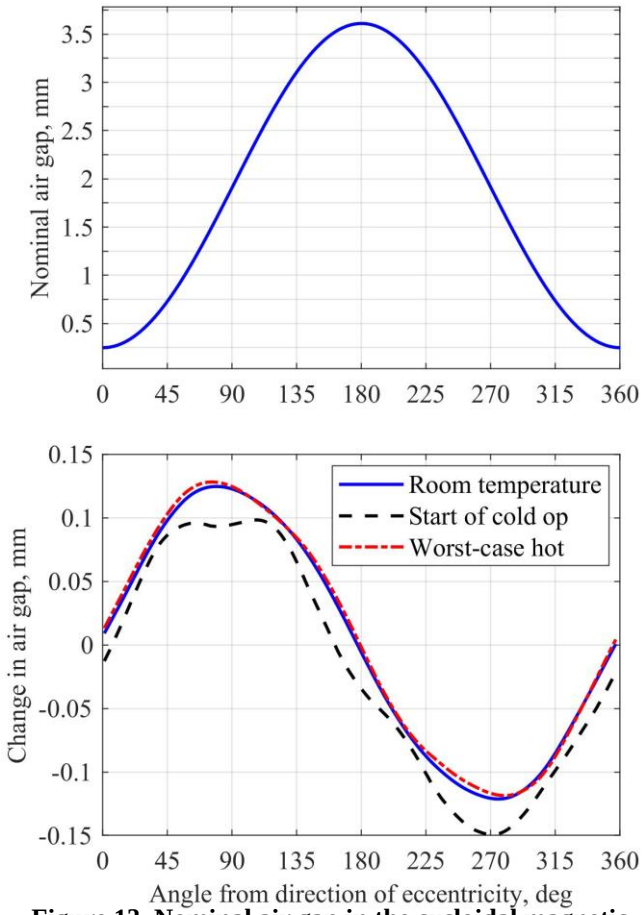

Figure 13. Nominal air gap in the cycloidal magnetic gear (top) and the deviation in air gap caused by structural deformation at peak output torque (bottom).

Table 5. Predicted life of the dry film lubricant in the bearings of the preliminary magnetically-geared actuator.

	Bearing							
	1	**2**	**3**	**4**	**5**	**6**	**7-14**	**15**
Revolutions (x 10^6)	8.7	8.8	25.7	0.56	0.18	0.44	0.41	0.44
% of threshold actuator life	250	273	796	217	68	167	159	7333
% of goal actuator life	30	33	96	26	8	20	19	880

actuator beyond the MDECE Project. Ongoing work in the development of the actuator focuses primarily on solving this issue without increasing the weight of the actuator significantly.

Future structural analysis will focus on reducing the mass of the design and quantifying loads due to transient thermal conditions. Additionally, in the development of the proof-of-concept version of the actuator, it was found that the zero load torque condition resulted in considerably more radial deformation in the direction of minimum air gap. Thus, the air gap is found to be smallest for zero output torque. This result is counterintuitive but occurs because (a) the magnets in the cycloidal gear fully interact at all times, (b) the magnetic forces shift from primarily torsional to purely radial with a net force toward the minimum air gap as the output torque decreases from its peak to zero, and (c) the magnetic forces on the eccentric rotor remain large at zero torque (as evidenced by Figure 3. Zero load torque conditions will be included in all future structural analysis for the actuator.

7. CONCLUSIONS

This paper presented the detailed design of a magnetically-geared actuator for use in extremely cold space environments. The requirements of the actuator, initial electromechanical design, thermal analysis, additional electromagnetic analysis, and structural analysis were presented.

The analysis results obtained to date indicate that the proposed magnetically-geared actuator is viable for lunar surface operation at temperatures down to 30 K (-243 °C). Material limits are not exceeded at the temperature extremes or peak loads, temperature gradients and differential thermal contractions are manageable, and the expected change in performance over the predicted internal temperature envelope (25 K (-248 °C) to 430 K (157 °C)) is acceptably small.

The selected preliminary design has a mass of 3.74 kg and efficiency of 83.9% based on the predictions of a design and optimization code that includes torque margins. The gear is predicted to be 2.85 kg with a continuous efficiency of 91.9%, whereas the motor is predicted to be 0.89 kg with a continuous efficiency of 91.3%. The total efficiency is higher than both the threshold and goal values of the project's key performance parameter on efficiency. After adding details to the design based on structural analysis and mechanical design, the predicted total mass increased to 5.01 kg. This mass is larger than the target maximum mass primarily due to the challenge of achieving the mass target while meeting the desired bearing life target. Corrections to the bearing sizing method in the design and optimization code of the cycloidal magnetic gear have been implemented to account for the increase in mass relative to the preliminary design. In future work, a more thorough mass optimization of the structure will be completed, and design modifications that reduce the bearing loads will be considered.

A proof-of-concept prototype has been designed in parallel with the work reported herein. Assembly of the hardware is expected to be completed in early Spring 2023. Functionality and performance of the prototype will be tested in an Earth ambient environment. Following a critical design review of the magnetically-geared actuator (planned for mid-Spring 2023), a fully functional prototype will be built and then ground tested in a relevant cryogenic-vacuum-dust environment in 2024.

ACKNOWLEDGEMENTS

This work was supported by the Motors for Dusty & Extremely Cold Environments (MDECE) Project within NASA's Game Changing Development Program and the Space Technology Mission Directorate.

REFERENCES

[1] Scheidler, J. et al., "The Impacts of Heating Actuators in Extremely Cold Space Environments," In Proc. of 2022 IEEE Aerospace Conference, pp. 1-8, 2022, doi: 10.1109/AERO53065.2022.9843758.

[2] ESR Technology Ltd., "Space Tribology Handbook," 5th Ed., 2013.

[3] Montbach, E. and Scheidler, J., "FY22 Motors For Dusty And Extremely Cold Environments (MDECE) Annual Review Presentation," 2022.

[4] Wang, Y. et al., "A Review on Magnetic Gears: Topologies, Computational Models, and Design Aspects," IEEE Transactions on Industry Applications, 55(5), pp. 4557-4566, 2019, doi: 10.1109/TIA.2019.2916765.

[5] Santiso-Zelaia, J. et al., "Design of Magnetic Gears for Space Applications," In Proc. of the 10th International

Conference on Power Electronics, Machines and Drives, pp. 182-187, 2020, doi: 10.1049/icp.2021.1165.

[6] Praslicka, B. et al., "Practical Analysis and Design of a 50:1 Cycloidal Magnetic Gear with Balanced Off-Axis Moments and a High Specific Torque for Lunar Robots," In Proc. of 2021 IEEE International Electric Machines & Drives Conference, pp. 1-8, 2021, doi: 10.1109/IEMDC47953.2021.9449504.

[7] Esnoz-Larraya, J. et al., "Optimagdrive: High-Performance Magnetic Gears Development for Space Applications," In Proc. of 17th European Space Mechanisms and Tribology Symposium, pp. 1-5, 2017.

[8] Perez-Diaz, J.L. et al., "Performance of Magnetic-Superconductor Non-Contact Harmonic Drive for Cryogenic Space Applications," Machines, 3(3), pp. 138-156, 2015, doi: 10.3390/machines3030138.

[9] SLS-SPEC-159, "Cross-Program Design Specification for Natural Environment (DSNE)", Rev G, 2019.

[10] Williams, J.-P. et al., "Seasonal Polar Temperatures on the Moon," Journal of Geophysical Research: Planets, 124(10), pp. 2505-2521, 2019, doi: 10.1029/2019JE006028.

[11] Zhang, J.A. and Paige, D.A., "Cold-trapped organic compounds at the poles of the Moon and Mercury: Implications for origins," Geophysical Research Letters, 36(16), 2009, doi: 10.1029/2009GL038614.

[12] Lunar Reconnaissance Orbiter data from Lunar QuickMap (https://quickmap.lroc.asu.edu).

[13] Arnold Magnetic Technologies, "Using Permanent Magnets at Low Temperature," Technical Note TN 0302, 2015.

[14] Hasegawa, M. et al., "Rare earth magnets for applications over a wide temperature range," Journal of Magnetism and Magnetic Materials, 124(3), pp. 325-329, 1993, doi: 10.1016/0304-8853(93)90134-N.

[15] Liu, J. et al., "Thermal Stability and Radiation Resistance of Sm-Co Based Permanent Magnets," In Proc. of Space Nuclear Conference, 2036, pp. 1-9, 2007.

[16] Gerber, S. and Wang, R.-J., "Analysis of the end-effects in magnetic gears and magnetically geared machines," In Proc. of 2014 International Conference on Electrical Machines, pp. 396-402, 2014, doi: 10.1109/ICELMACH.2014.6960211.

[17] HLS-UG-001, "Lunar Thermal Analysis Guidebook," 2021.

[18] Anderson, M.J., "The Thermal Conductance of Solid-Lubricated Bearings at Cryogenic Temperatures in Vacuum," In Proc. of 30th Aerospace Mechanisms Symposium, pp. 31-45, 1996.

[19] NASA-STD-5001B, "Structural Design and Test Factors of Safety for Spaceflight Hardware," Rev B with change 2, 2016.

[20] Tallerico, T.F. et al., "Outer Stator Magnetically-Geared Motors for Electrified Urban Air Mobility Vehicles," In Proc. of 2020 AIAA/IEEE Electric Aircraft Technologies Symposium (EATS), 2020, doi: 10.2514/6.2020-3563.

BIOGRAPHY

Justin Scheidler *received his B.S. and Ph.D. degrees in Mechanical Engineering from The Ohio State University in 2011 and 2015. He has been with NASA GRC for 7 years. He is the Project Lead Engineer of the Motors for Dusty & Extremely Cold Environments (MDECE) Project. He has conducted research on traditional and superconducting electric machines, magnetic gears, and smart material-based vibration control technologies.*

Thomas Tallerico *received his B.S. and M.S. degrees in Mechanical Engineering and Applied Mechanics from the University of Pennsylvania in 2015 and 2016. He has been an aerospace research engineer at NASA GRC for 6 years. His research areas include magnetic gears, electric motors, and very high cycle material fatigue.*

Aaron Anderson *received his B.S from Purdue University West Lafayette in 2017 and M.S. from the University of Illinois at Urbana-Champaign in 2020. He has been at NASA GRC for 2 years. He is the electrical engineer for the Motors for Dusty & Extremely Cold Environments (MDECE) Project. In addition, he works on electric motor analysis and design for electrified aircraft propulsion.*

Steven Darmon *received his B.S. in Mechanical Engineering from Ohio Northern University in 2009. He worked as an affiliate contractor for NASA GRC for 1 year. He served as the thermal analyst for the Motors for Dusty & Extremely Cold Environments (MDECE) Project. He specializes in industrial refrigeration, fluid mechanics, and heat transfer analysis.*

Peter Hoge *received his B.S. degree in Mechanical Engineering from The University of Akron and his M.S. degree from Case Western Reserve University. He has performed structural analyses for over 30 years on numerous spaceflight, aerospace, and defense related projects.*

Kyle Whitling *is a Senior Mechanical Engineer with HX5 with 20 years of Aerospace Engineering experience. He has designed, built and qualified components on the Boeing 737, Bell 525 Helicopter, and microgravity experiments that operate in the International Space Station. He is a graduate of Case Western Reserve University with a B.S. degree in Mechanical Engineering and M.S. in Engineering Management.*

Jesse Hawk *received his A.S. in Drafting and Design from El Paso Community College in 2007. He has been a Mechanical Designer for over 10 years and supported NASA GRC since 2020.*

Erica Montbach *received her B.A. in Physics from The College of Wooster and her Ph.D. in Chemical Physics from The Liquid Crystal Institute at Kent State University. She is the Project Manager of the Motors for Dusty & Extremely Cold Environments (MDECE) Project. Dr. Montbach is responsible for leading multi-disciplinary teams to develop solutions for a sustained presence on the Moon as the project manager for Lunar Dust Mitigation (DM) and In-Situ Resource Utilization (ISRU) portfolios for Glenn Research Center.*